ACS NANO
Cite This: ACS Nano 2019, 13, 1772−1783
www.acsnano.org

ARTICLE

High-Performance All-Inorganic $CsPbCl_3$ Perovskite Nanocrystal Photodetectors with Superior Stability

Maogang Gong,*,† Ridwan Sakidja,‡ Ryan Goul,† Dan Ewing,§ Matthew Casper,§ Alex Stramel,§ Alan Elliot,§ and Judy Z. Wu*,†

†Department of Physics and Astronomy, University of Kansas, Lawrence, Kansas 66045, United States
‡Department of Physics, Astronomy, and Materials Science, Missouri State University, Springfield, Missouri 65897, United States
§Department of Energy's National Security Campus, Kansas City, Missouri 64147, United States

Supporting Information

ABSTRACT: All-inorganic perovskites nanostructures, such as $CsPbCl_3$ nanocrystals (NCs), are promising in many applications including light-emitting diodes, photovoltaics, and photodetectors. Despite the impressive performance that was demonstrated, a critical issue remains due to the instability of the perovskites in ambient. Herein, we report a method of passivating crystalline $CsPbCl_3$ NC surfaces with 3-mercaptopropionic acid (MPA), and superior ambient stability is achieved. The printing of these colloidal NCs on the channel of graphene field-effect transistors (GFETs) on solid Si/SiO_2 and flexible polyethylene terephthalate substrates was carried out to obtain $CsPbCl_3$ NCs/GFET heterojunction photodetectors for flexible and visible-blind ultraviolet detection at wavelength below 400 nm. Besides ambient stability, the additional benefits of passivating surface charge trapping by the defects on $CsPbCl_3$ NCs and facilitating high-efficiency charge transfer between the $CsPbCl_3$ NCs and graphene were provided by MPA. Extraordinary optoelectronic performance was obtained on the $CsPbCl_3$ NCs/graphene devices including a high ultraviolet responsivity exceeding 10^6 A/W, a high detectivity of 2×10^{13} Jones, a fast photoresponse time of 0.3 s, and ambient stability with less than 10% degradation of photoresponse after 2400 h. This result demonstrates the crucial importance of the perovskite NC surface passivation not only to the performance but also to the stability of the perovskite optoelectronic devices.

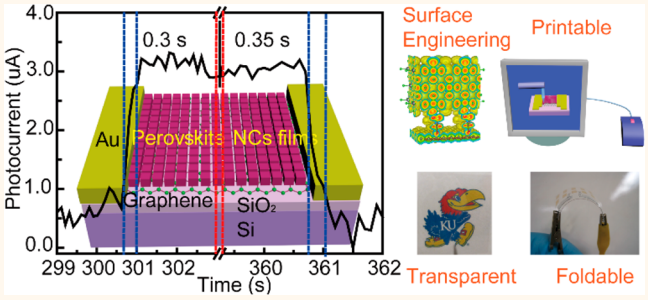

KEYWORDS: *perovskite nanocrystals, stability, surface engineering, visible-blind ultraviolet photodetector*

Recently, organic, inorganic, or hybrid perovskites have attracted extensive research interest due to their superior properties and potential application in optoelectronic devices.[1−5] However, the instability caused by the inevitable volatilization and decomposition of organic components within the hybrid perovskites must be addressed before realization of practical application.[6,7] Compared with the organohalide perovskites, the all-inorganic counterparts have excellent crystallinity with a smaller detrimental effect of grain boundaries, which results in improved stability and bandgap tunability.[6−8] After Kovalenko *et al.* reported successful fabrication of nanocrystals (NCs) of inorganic cesium lead halide perovskite ($CsPbX_3$, where X is Cl, Br, and I),[8] the inorganic $CsPbX_3$ NCs have gained interest and have been widely developed in many high-performance optoelectronic devices, such as light-emitting diodes,[9−13] lasers,[14−16] solar cells,[17,18] and photodetectors.[19,20] Furthermore, the solution processed colloidal $CsPbX_3$ NCs provide the merits of being low-cost, soluble, and printable.[6,15,21]

Despite the exciting progress made in the fabrication and characterization of $CsPbX_3$ NCs-based optoelectronic devices, the device performance especially stability is far from meeting the application requirements.[22−28] One of the important factors is the intrinsic dynamic chemical instability of $CsPbX_3$ NCs induced by the active nature of the chemical bonding between the long-chain capping ligands and the inorganic surface.[29−31] Furthermore, the solution synthesis process introduces capping ligands, such as 1-octadecene (ODE), oleic acid (OA), and oleylamine (OLA), which form an insulating layer on the surface of the $CsPbX_3$ NCs and block

Received: October 14, 2018
Accepted: January 28, 2019
Published: January 28, 2019

DOI: 10.1021/acsnano.8b07850
ACS Nano 2019, 13, 1772−1783

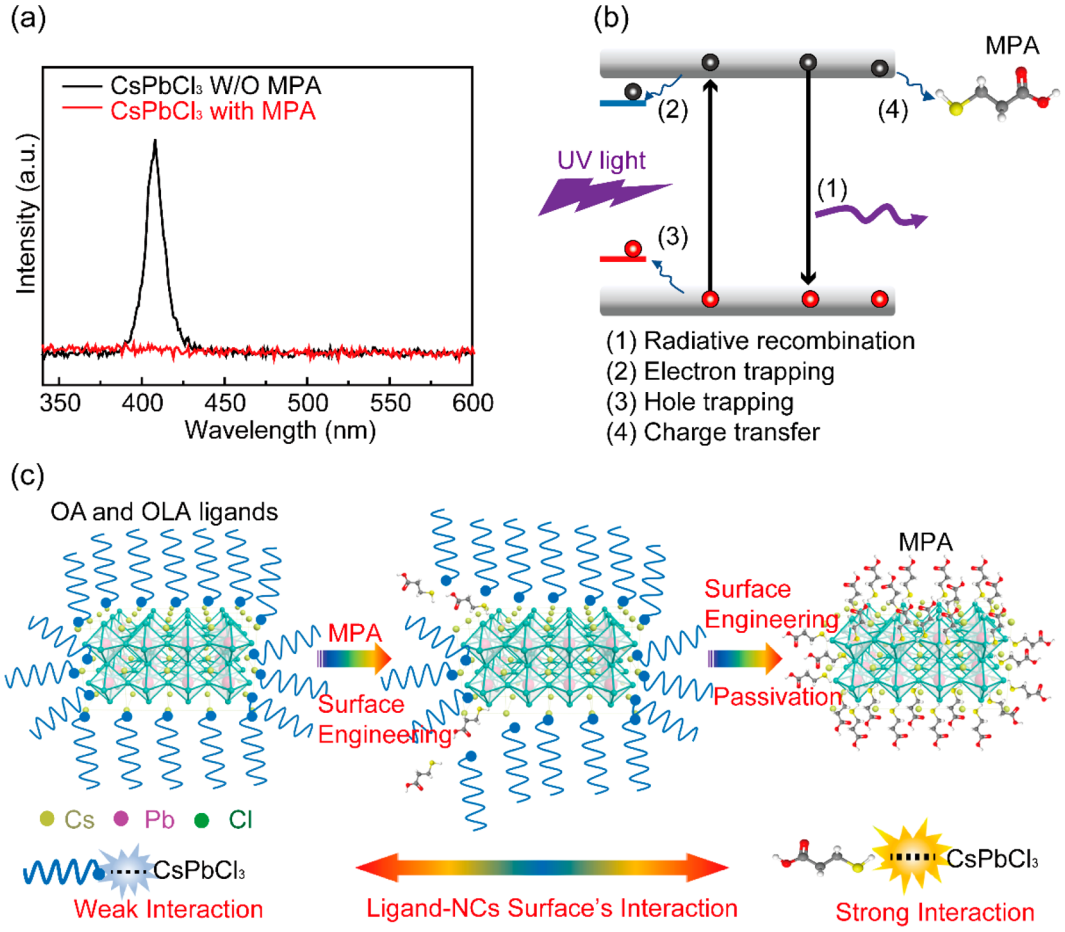

Figure 1. (a) Comparison of PL emission spectra of $CsPbCl_3$ NCs as synthesized (black) and after the MPA ligand exchange (red) in hexane; the PL quenching is a signature of the excited electrons transfer to the MPA ligands. (b) Competing dynamic relaxation processes in $CsPbCl_3$ NCs upon photon excitation with an UV light. (c) Schematic description of the surface passivation process in which the weak-interaction OA, OLA, and ODE ligands on as-synthesized $CsPbCl_3$ NCs are replaced by the strong-interaction MPA ligands on the $CsPbCl_3$ NCs, resulting in both superior stability of the $CsPbCl_3$ NCs and high charge-transfer efficiency from the MPAs of excellent electrical conductivity.

the carrier transport and injection at the interface of the $CsPbX_3$ NCs and other components in the optoelectronic devices. Charge carrier transport is a key step in optoelectronic devices, which directly determines the performance of the device including both sensitivity (quantum efficiency) and response speed. The semiconducting or insulating alkyl chain ligands introduced in the growth of colloidal $CsPbCl_3$ NCs is well-known as the barrier of charge transfer. In addition, the weak connection between the alkyl chain ligands and the surface of NCs can cause ligand loss in purification process and even in storage stage of the NCs.[32−34] The exposed surface of the perovskite NCs is prone to degradation in ambient, resulting in instability of the perovskite NCs in ambient conditions. Thereafter, the surface engineering replacing the insulating and unstable layer on the $CsPbX_3$ NCs becomes critically important in perovskite-NC-based optoelectronic devices. A variety of methods and strategies have been developed to address this issue, including adding molecular additives in colloidal solutions of NCs,[23−25] and embedding the NCs into a chemically stable, amorphous, oxygen- and water-impermeable glass matrix.[26−28] However, limitations of these approaches remain. For example, the added molecular additives[23−25,35] are normally movable and prone to be separated from the surface of the NCs instead of forming a uniform surface protective coating on the $CsPbX_3$ NCs.[36] However, those glass matrix strategies can somewhat solve the stability problem but limit the application in a narrow emitting area. In particular, passivation of the $CsPbX_3$ NCs with insulating molecules or a glass matrix would block charge transfer between the $CsPbX_3$ NCs and the other device components in the optoelectronic devices and cannot be employed for optoelectronics that rely on such charge transfer. Therefore, it is imperative to address the critical need for a NCs' surface engineering to not only protect the $CsPbX_3$ NCs for their ambient stability but also facilitate the highly efficient charge transfer required for optoelectronic applications.[25]

Herein, a robust surface-engineering strategy is reported on inorganic perovskite $CsPbCl_3$ NCs using a thiol (3-mercaptopropionic acid, MPA) passivating process. We show such a surface engineering can not only facilitate high-efficiency charge transfer between $CsPbCl_3$ NCs and graphene in field-effect transistors (GFETs) but also passivate the NCs' surface to minimize the charge trapping and prevent degradation of the $CsPbCl_3$ NCs in ambient conditions. Excitingly, these engineered $CsPbCl_3$ NCs/GFET photodetector devices with a van der Waals (vdW) heterojunction interface demonstrate ultrahigh visible-blind UV responsivity exceeding 10^6 A/W, high detectivity up to 2×10^{13} Jones, and

DOI: 10.1021/acsnano.8b07850
ACS Nano 2019, 13, 1772−1783

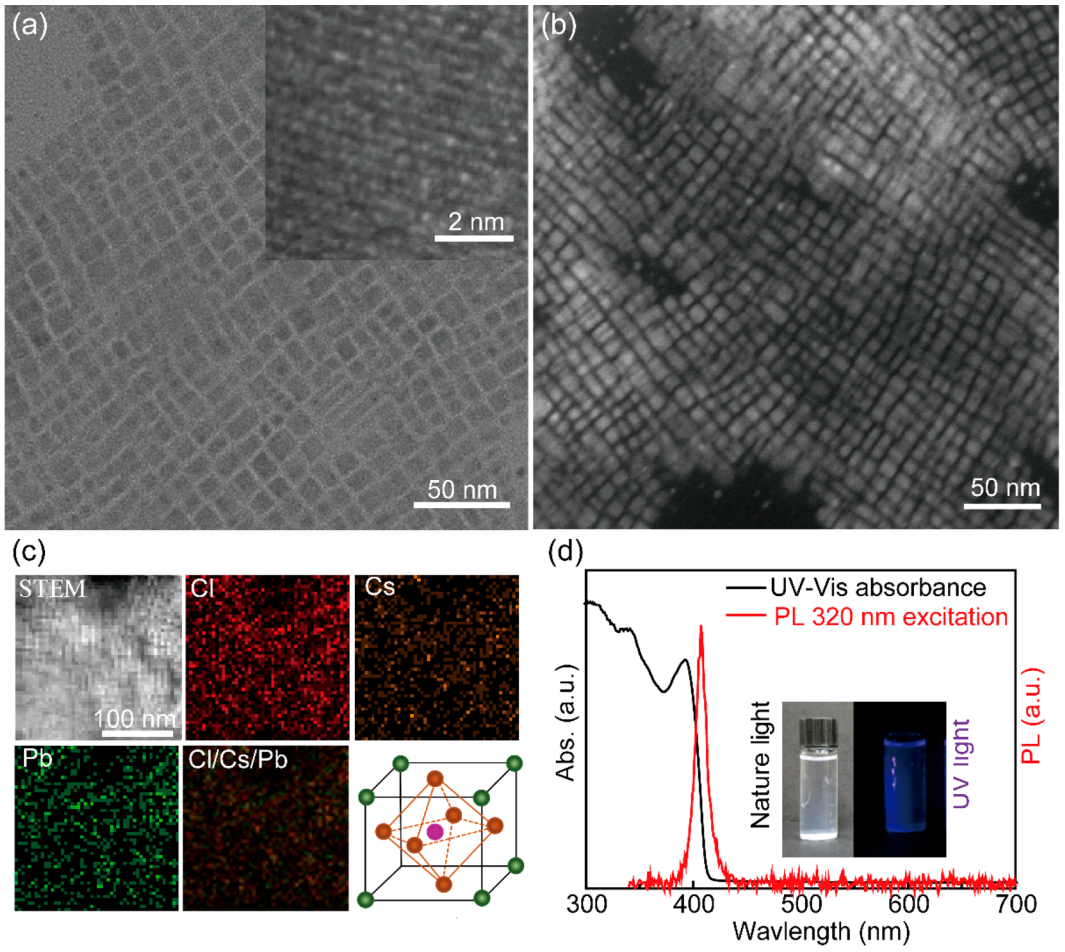

Figure 2. (a) TEM and HRTEM (inset) images of $CsPbCl_3$ NCs. (b) High-angle annular dark field scanning TEM image of $CsPbCl_3$ NCs. (c) STEM image of $CsPbCl_3$ NCs and the corresponding EDS element maps of Cl, Cs, and Pb and the combination Cs/Pb/Cl on the same area, together with a schematic illustration of the $CsPbCl_3$ with identical octahedral coordination environment of host cation formed by six halide atoms. (d) UV−vis absorption and PL spectra upon excitation at 320 nm of the $CsPbCl_3$ NCs. The insets are photos of $CsPbCl_3$ NCs in hexane solution under natural light (left) and 360 nm UV light (right), respectively.

a fast photoresponse time of 0.3 s. In particular, we show that the $CsPbCl_3$ NCs/GFET photodetectors can be stable, exceeding 2400 h under ambient conditions, making them robust and promising for practical applications.

RESULTS AND DISCUSSION

Figure 1a compares the photoluminescence (PL) spectra of $CsPbCl_3$ NCs without and with ligand exchange and passivation via MPA. The as-synthesized $CsPbCl_3$ NCs exhibit strong PL properties with a prominent PL peak at 407 nm, coming from the radiative electron−hole pair combination in the $CsPbCl_3$ NCs. The narrow emission line width of 11.3 nm at the full width at half-maximum (fwhm) is indicative of the high crystallinity of the $CsPbCl_3$ NCs (Figure 1a). The strong PL emission observed in the as-synthesized $CsPbCl_3$ NCs is anticipated from the insulating (OA and OLA) ligands layer on the surface of the NCs. In a sharp contrast, the PL peak disappeared in the surface-engineered $CsPbCl_3$ NCs after the MPA ligands exchange and passivation, confirming that the MPA ligands replace the initial alkyl ligands attached on the NC surfaces and provide an excellent charge-transfer pathway and, hence, completely quenches the radiative electron−hole recombination.

Figure 1b shows the optoelectronic processes in $CsPbCl_3$ NCs before and after the surface engineering with an MPA passivation. The three mechanisms of radiative recombination (1), electron trapping (2), and hole trapping (3) typically occur in $CsPbCl_3$ NCs or other semiconductor NCs. The charge-trapping mechanisms due to surface defects and other impurity states of the NCs are particularly harmful to optoelectronics illustrating typically in reduced photocurrents and slow photoresponse. The implementation of the passivation *via* MPA (4) with thiol ligands provides an efficient pathway through which to resolve such issues. This is primarily because the MPA passivation provides three distinctive advantages. First, it passivates the surface of the $CsPbCl_3$ NCs to minimize the charge trapping, which can lead to faster photoresponse and higher photoresponsivity.[37−39] In addition, the surface defects and weak ligands−NCs interaction are prone to instability and degradation of the $CsPbCl_3$ NCs or most semiconductor nanostructures in ambient conditions, resulting in the degradation of the NCs, typically within a few hours to a few days. The MPA passivation of the $CsPbCl_3$ NC surface provides a solution to the degradation problem. Finally, MPA itself has a short thiol ligand can offer a highly efficient carrier-transfer avenue from $CsPbCl_3$ NCs to acceptors, such as graphene, which is critical

DOI: 10.1021/acsnano.8b07850
ACS Nano 2019, 13, 1772−1783

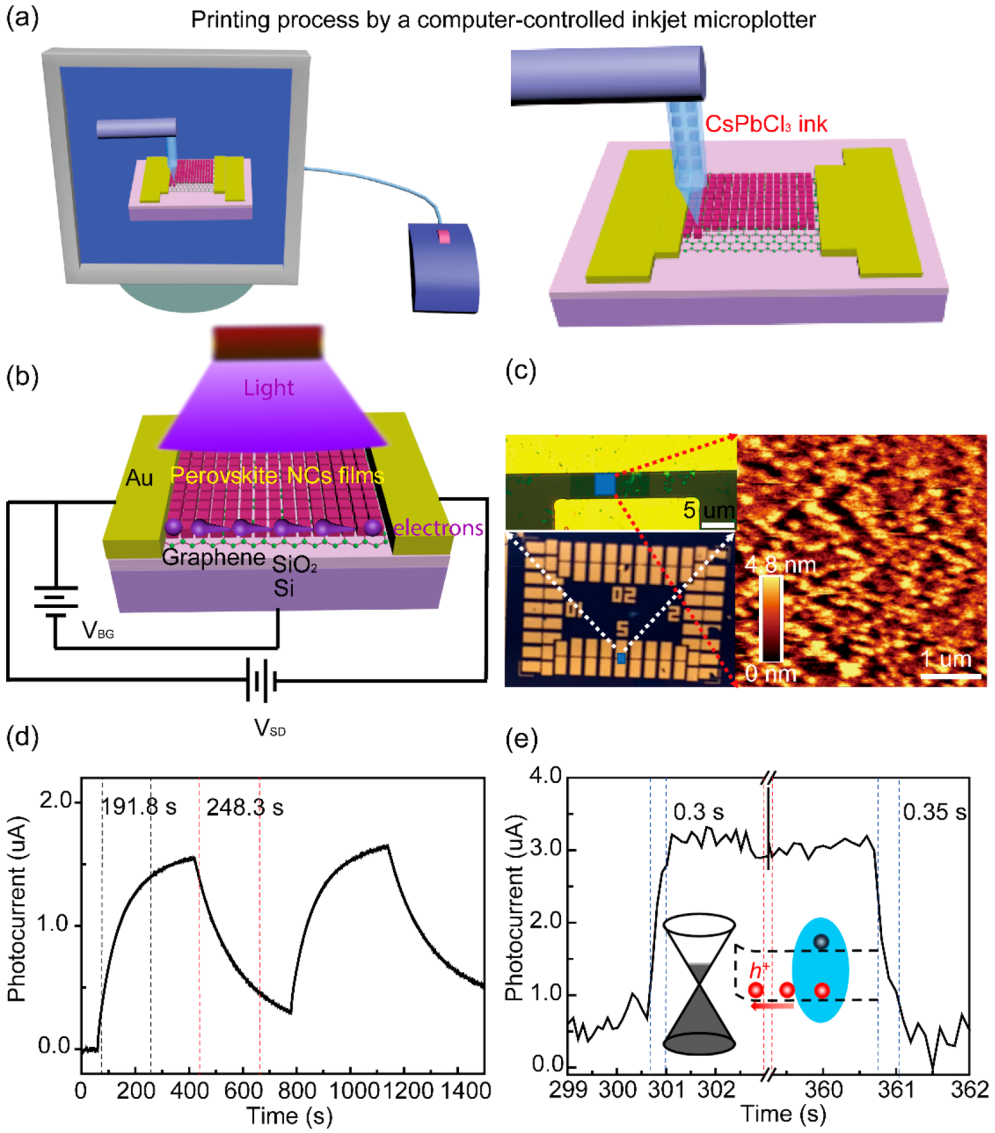

Figure 3. (a) Schematic of computer controlled printable process. (b) Schematic of the $CsPbCl_3$ NCs/GFET photodetector under UV illumination. (c) A digital photograph of a GFET chip with 36 GFETs of different designed graphene with the same channel width of 20 μm and different channel lengths of 2, 5, 10, and 20 μm as labeled. Top: a zoomed-in optical microscope view of a $CsPbCl_3$ NCs/GFET device with a 5 μm channel length. The right image is an AFM image of the $CsPbCl_3$ on the GFET channel. Time domain photoresponse of the $CsPbCl_3$ NCs/GFET device to 400 nm wavelength excitation (d) before and (e) after the MPA treatment. The light intensity and source-drain bias voltage are 8.17 $\mu W/cm^2$ and 0.2 V, respectively. The GFET channel is 4.0 μm (length) × 12.1 μm (width). The inset of Figure 3e shows the energy level diagram of the $CsPbCl_3$ NCs/GFET vdW heterojunctions and charge-transfer process under illumination.

to high-performance optoelectronics based on the $CsPbCl_3$ NCs. This argument is supported by the complete quench of the PL in the $CsPbCl_3$ NCs after the MPA passivation shown in Figure 1a and density function theory (DFT) simulations to be detailed in the following. Accordingly, the distinction in the exciton relaxation dynamics in the $CsPbCl_3$ NCs before and after the MPA passivation has a significant impact on the dynamics of the optoelectronic process and, therefore, the performance of the $CsPbCl_3$ NCs-based optoelectronic devices. To examine the integrity of the $CsPbCl_3$ NCs, SEM images before and after the MPA ligand exchange are demonstrated in Figure S1. The $CsPbCl_3$ NCs seem intact based on the negligible variations in the morphology of the $CsPbCl_3$ NCs.

On the basis of the above analysis, the prominent role of the MPA ligands on the $CsPbCl_3$ NCs is illustrated in Figure 1c. The original $CsPbCl_3$ NCs are capped by the organic ligands (OA and OLA) and exhibit some extent stability only in the organic reagent environment. While OA and OLA ligands play an important role as surface-chelating ligands, they can easily be removed in the purification process of the $CsPbCl_3$ NCs or even during the storage due to their weak interaction (bonding) with the NCs.[32] The ligands loss surrounding the surface of $CsPbCl_3$ NCs leads the instability of the $CsPbCl_3$ NCs, or perovskite NCs in general, resulting in the perovskite NC degradation in ambient. When the organic OA and OLA ligands are replaced with MPA ligands, the strong interaction between negative HS^- ligands in MPA and the positively polarized Pb^{2+} terminating surface of the $CsPbCl_3$ NCs enables a strong bonding of the MPA ligands to the NC surface, which provides benefits of (1) enhanced ambient stability of the $CsPbCl_3$ NCs, (2) reduced charge trapping by the surface

DOI: 10.1021/acsnano.8b07850
ACS Nano 2019, 13, 1772−1783

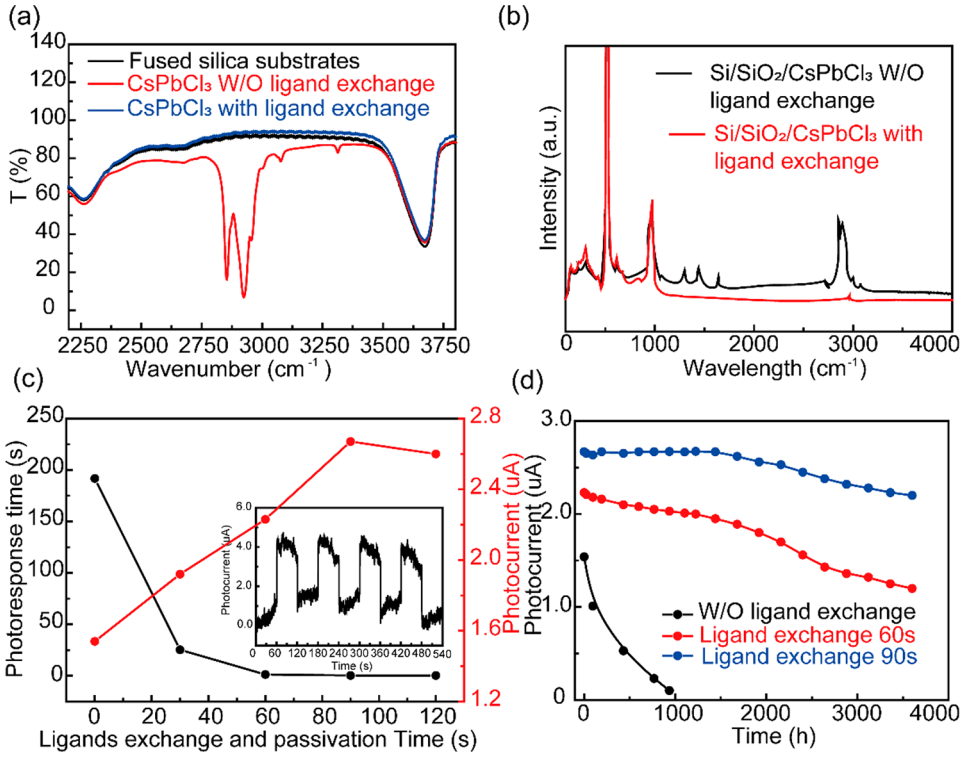

Figure 4. (a) FTIR spectra of $CsPbCl_3$ NCs before and after the MPA ligand exchange on transparent fused silica substrates. (b) Raman spectra of $CsPbCl_3$ NCs before and after the MPA ligand exchange on SiO_2/Si substrates. (c) The photoresponse time and photocurrent dependence on the MPA passivation time. The inset shows the dynamic photocurrent of the $CsPbCl_3$ NCs/GFET photodetector with passivation processing time of 90 s upon 400 nm and 8.17 $\mu W/cm^2$ illumination with four light on/off cycles. (d) Photocurrent measured on a $CsPbCl_3$ NCs/GFET photodetectors without and with passivation under ambient conditions.

defects of the $CsPbCl_3$ NCs, and (3) highly efficient charge transfer between $CsPbCl_3$ NCs and other functional materials through highly conductive MPA ligands. These will be demonstrated by the following simulation and experimental characterization of the $CsPbCl_3$ NCs/GFET photodetectors with and without the MPA passivation.

The transmission electron microscopy (TEM) images demonstrate that the obtained $CsPbCl_3$ NCs have an approximately cubic structure with an average size of 10.5 nm (Figure 2a). The inset shows a high-resolution TEM (HRTEM) image of the NC with a very clear lattice-fringes of 0.39 nm that matches well with that expected for the crystal plane of (110). The HRTEM image confirms the $CsPbCl_3$ NCs have high crystallinity, which is critical to optoelectronic device performance. The morphology and purity of $CsPbCl_3$ NCs were more conspicuous from dark-field scanning transmission electron microscopy (STEM) (Figure 2b). The STEM image combined with the energy-dispersive spectroscopy element mapping (Figure 2c) confirms the structure and elemental components of the $CsPbCl_3$ NCs. The composite images of Cs, Pb, and Cl show a uniform distribution of each of these elements incorporated into the $CsPbCl_3$ NCs. The schematic shows a perfect octahedral coordination structure of host Pb cations surrounded by six halide atoms for $CsPbCl_3$ NCs. Figure 2d display the UV–visible absorption spectrum (black) and PL spectrum (red) of the $CsPbCl_3$ NCs. The fwhm of the PL peak is ~11.3 nm, located at the wavelength of ~407 nm, which matches well with the absorption edge of $CsPbCl_3$ NCs in the absorption spectrum.

The schematic image of the vdW heterojunction $CsPbCl_3$ NCs/GFET device printing process is demonstrated in Figure 3a with the printing process detailed in the Methods section. The printing of $CsPbCl_3$ NCs in hexane on GFETs was carried out on a printer (SonoPlot, Inc.). Figure 3b demonstrates one of the $CsPbCl_3$ NCs/GFET vdW heterojunction photodetector with drain, source, and back-gate electrodes. The photodetector is composed of a GFET fabricated on monolayer graphene on Si/SiO_2 (90 nm in thickness as gate dielectric) substrate and a layer of printed $CsPbCl_3$ NCs (purple cubes) on the GFET channel of typical dimension of 4.0 μm × 12.1 μm (length × width) (see the Methods section). Figure 3c shows a digital image of GFET chip and a magnified optical image of one GFET device (top) taken from a chip of 36 GFETs. The atomic force microscopy (AFM) image taken on a representative $CsPbCl_3$ NCs/GFET device also shown in Figure 3c reveals a dense $CsPbCl_3$ NCs film covering the underside of the GFET channel. The thickness of this $CsPbCl_3$ NCs layer is around 10 nm (Figure S2). The root-mean-square (RMS) roughness of the $CsPbCl_3$ NCs film is 1.32 nm. Figure 3d,e demonstrates that the MPA treatment dramatically improves the performance of the $CsPbCl_3$ NCs/GFET photodetectors. The dynamic photoresponses are compared on photodetectors without (Figure 3d) and with (Figure 3e) the MPA treatment. The profound effect of the MPA treatment is demonstrated in the shortened photoresponse time and enhanced photocurrent ($I_{photo} = I_{light} - I_{dark}$). On the photodetector without the ligand treatment, the photoresponse time is ~191.8 s, which defines the time span 10%–90% of the photocurrent peak amplitude, and the photocurrent is around 1.54×10^{-6} A. The device treated with methanol only demonstrates the similar performance to that of the untreated device based on the photocurrent and response

DOI: 10.1021/acsnano.8b07850
ACS Nano 2019, 13, 1772–1783

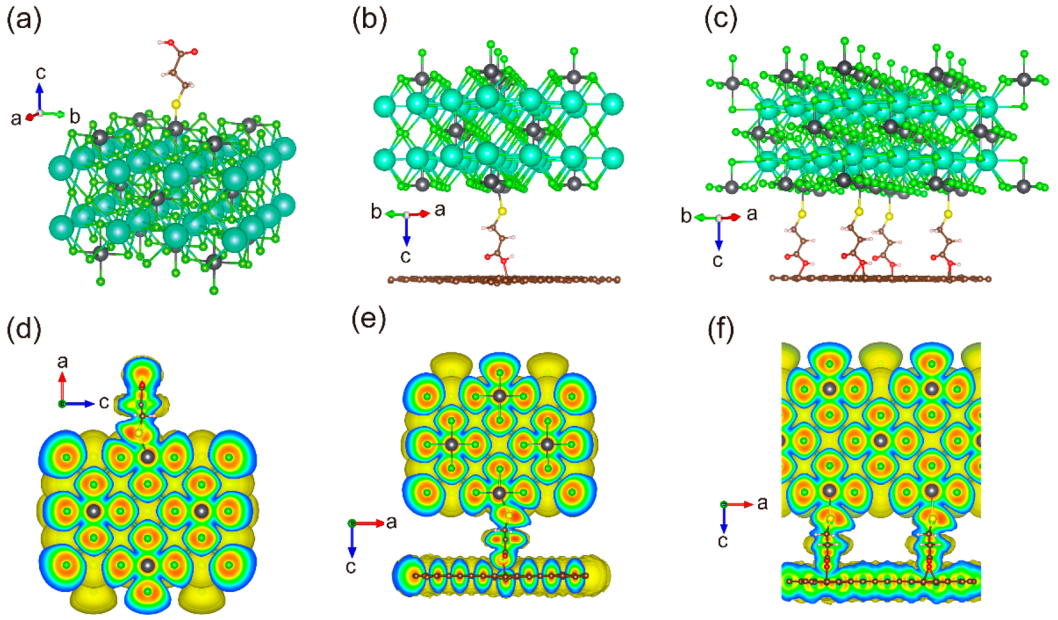

Figure 5. Atomic trajectories after the DFT relaxation calculations for a series of hybrid structures: (a) Pb-terminated $CsPbCl_3$ plus MPA, (b) Pb-terminated $CsPbCl_3$ plus MPA plus Graphene, and (c) Pb-terminated $CsPbCl_3$ plus 4MPA plus graphene. The electron localization function (ELF) plots after the DFT relaxation calculations for a series of hybrid structures: (d) Pb-terminated $CsPbCl_3$ plus MPA, (e) Pb-terminated $CsPbCl_3$ plus MPA plus graphene, and (f) Pb-terminated $CsPbCl_3$ plus 4MPA plus graphene. The MPA ligands are connecting on one side to the graphene and the other side toward the $CsPbCl_3$ NCs.

times (Figure S3). In particular, the slow response times on these devices are comparable to that reported earlier on the organometallic perovskite/PCBM bulk heterojunction photodetectors that exhibit a rising time of 92 s (0% to 70% of the I_{photo} peak amplitude) and decay time of 6203 s (100% to 30% of the I_{photo} peak amplitude) for the 1% [6,6]-phenyl-C61-butyric acid methyl ester (PCBM) devices.[40] In these organometallic perovskite/PCBM devices, the perovskite domains are surrounded by organic molecules of PCBM, which serve as the carrier traps and are responsible for the longer response times compared with the similar devices without PCBM. Moreover, considering the dramatic improvement of the response times by about 3 orders of magnitude with the MPA ligand exchange, we argue that the long response time in the $CsPbCl_3$ NCs/graphene photodetectors is primarily due to the non-optimal surface of the NCs and their interface with graphene; both can cause serious charge trapping and, hence, slow photoresponse. The improvement in the photoresponse and response times by the MPA ligand exchange supports this argument and suggests that the performance can be further improved with optimal engineering of perovskite NCs surface and their interface with graphene. The I_{photo} was increased by >73.3% to 2.67×10^{-6} A in the photodetector with the MPA ligand treatment. Furthermore, the photoresponse of the $CsPbCl_3$ NCs/GFET vdW heterojunction devices is significantly faster after the MPA passivation. The rise time (0.3 s) and fall time (0.35 s) are reasonably symmetric, with a slightly longer fall time that may be attributed to some minor charge-trapping mechanisms. It should be noted that these response times are about 2 orders of magnitude shorter than that in the prior reports of similar devices based on organic or organic−inorganic hybrid perovskite films and NCs,[40,41] illustrating the importance of the surface engineering on the performance of the $CsPbCl_3$ NCs-based optoelectronic devices. It also confirms the benefits of the ligand exchange in removing the charge-transfer blocking and trapping layer from the long-chain carbonate on the surface of the $CsPbCl_3$ NCs.

The completeness of the MPA ligand processing and passivation can be certified by characterizing the C−H bond stretch intensity of OA and OLA using Fourier-transform infrared (FTIR) spectroscopy (Figure 4a).[42] The success of the ligand exchange strategy can be attributed to the relative weak bonds between NCs and OA/OLA compared to the thiol bond connection to the NCs. Figure 4b shows the Raman signature spectra of $CsPbCl_3$ NCs without and with ligand exchange. The bands associated with the OA/OLA at 1301, 1441, and 1523 cm^{-1} are observed in as-synthesized $CsPbCl_3$ NCs (black curve). The band at 1301 cm^{-1} is due to the C−H bending twist mode in the $-CH_2$ group, while the band at 1441 cm^{-1} comes from the CH_2 and CH_3 bending or scissoring motions, and the band at 1523 cm^{-1} is ascribed to the C−C−C stretching mode.[43,44] Additionally, the observation of additional group bands in the higher wave-number range (2800−3100 cm^{-1}) come from the C−H stretching modes.[45] It is noted that all of the C−H and C−C−C vibrational band peaks related with OA/OLA are disappeared after ligand exchange via MPA (red curve). The Raman spectra well confirm the completeness of the ligand exchange procedure. The Raman signatures are well consistent with the FTIR spectra (Figure 4a), indicating the success of the ligand exchange process. Figure 4c demonstrates the photoresponse time and photocurrent dependence on the ligand exchange and passivation time. The photoresponse time dramatically decreases from 192.8 s without ligand passivation to 0.25 s with 120 s passivation. Accordingly, the photocurrents monotonically increase from 1.54 μA without passivation to 2.67 μA passivation processing time 90s, followed with a slight decrease at a longer passivation time from 90s to 120s. The slight decrease in photocurrent can be attributed to minor $CsPbCl_3$ NCs peeling off from the graphene surface.[37] The photocurrent of 2.6 μA at a

DOI: 10.1021/acsnano.8b07850
ACS Nano 2019, 13, 1772−1783

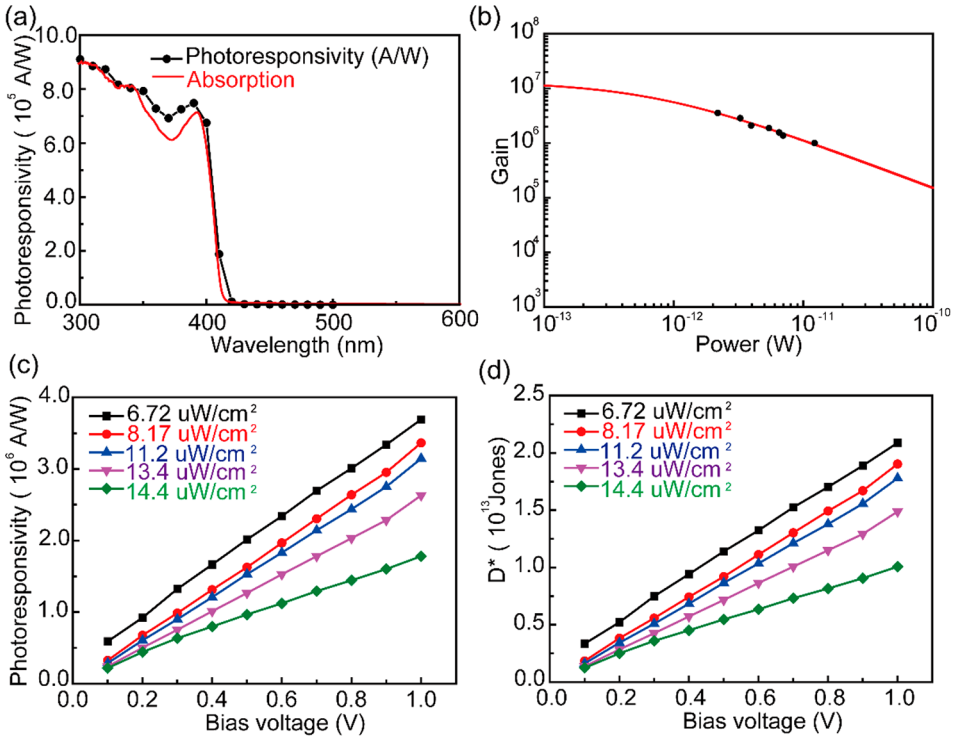

Figure 6. (a) Spectral photoresponsivity of the $CsPbCl_3$ NC/GFET photodetectors. (b) Photoconductive gain *vs* illumination power measured experimentally (black dots) and theoretical fitting (red curve). (c, d) Photoresponsivity and detectivity as a function of the bias voltage under different light intensity and wavelength of 400 nm.

passivation time of 120 s is 16% higher than the 2.23 μA at a passivation time of 60 s. The longer passivation time of 120 s also results in the fastest response time of 0.25 s in contrast to 1.2 s on the device with passivation time of 60 s. Therefore, the optimal passivation time is around 90 s. The inset of Figure 4c shows the dynamic photocurrent of a $CsPbCl_3$ NCs/GFET vdW heterojunction device to the light ON/OFF at the bias voltage of 0.2 V. After more than four "on/off" light cycles, a stable current density level was maintained, illustrating photodetection reversibility of the device. In addition, an effect of the MPA passivation is illustrated in the stability of the device performance tested for 2400 h. As shown in Figure 4d, the photocurrent of a $CsPbCl_3$ NCs/GFET vdW heterojunction device without MPA ligand passivation dramatically decreased by more than 50% of its initial value after about 800 h. In contrast, the MPA passivated device with a 90 s passivating time demonstrates superior ambient stability with only 8.2% reduction of the photocurrent after 2400 h.

A theoretical simulation was carried out to shed light on the passivating mechanisms of the MPA ligands and the role of the ligands on the charge transfer across the interface of $CsPbCl_3$ NCs/GFET and on the stabilization of $CsPbCl_3$ NCs. We tested a number of scenarios by which the NCs can possibly be connected to the MPA based on the variations of the terminating surface, namely the Pb^{2+} cation and Cl^- anion on the (001) surfaces in Figures 5 and S4. With respect to the Pb^{2+} cation, the connectivity could be bridged by the S^{2-} anion, whereas to the Cl^- anion, a possible connectivity with HS end member of the MPA linker exists. In both cases, the OH^- end member of MPA linker is directed toward the graphene. We did not consider the last alternative, which is the Cs^+, due to the likelihood that its higher electron affinity (46 kJ/mol *vs* 34 kJ/mol for Pb) will result in the Cl^- ionic capping at a hypothetical Cs^+ terminating surface. The scenario from which the Pb terminating surface connects with the S^{2-} ligand (after deprotonation within the solution) appears to be the more likely possibility especially under an acidic solution from which deprotonation of the thiol group will yield the negatively charged sulfur end member. The Supporting Information provides further details on our approach to arrive at this conclusion. Figure 5a shows the relaxed structure of the $CsPbCl_3$ NCs with the MPA ligands on the NC surfaces. The more likely scenario is that the MPA forms bonds with the positively polarized Pb capping the surface of the $CsPbX_3$ NCs. The MPA ligands attached to the surface of the $CsPbCl_3$ NCs play a critical role in the passivation of the NCs surface through the formation of the Pb−S bonds. In addition, the NCs−MPA−graphene connection motivates an increase in the electron delocalization, indicative of the formation of the bridge bond as shown in Figure 5b,c of the $CsPbCl_3$ NCs/graphene vdW heterojunction structures composed of one (Figure 5b) and four (Figure 5c) MPA ligands connected on one side to the graphene and the other side to the $CsPbCl_3$ NCs. Figure 5d−f shows the trajectory of the hybrid structure showing the relative configuration stability of the connections by the MPA ligands toward both ends. This leads to two beneficial effects: preventing the degradation of the $CsPbCl_3$ NCs and reducing charge trapping by the intrinsic surface defects such as dangling bonds. Table S1 lists the Bader charge of the relevant species on the two scenarios considered; Pb (linked to MPA), S (linked to $CsPbCl_3$), Cl (linked to MPA), H (linked to $CsPbCl_3$), O (linked to the graphene sheet), and the average charge or atom of the graphene sheet, supporting the charge connectivity from $CsPbCl_3$ to the graphene by MPA ligands. The presence of MPA linkers between the $CsPbCl_3$ NC and graphene provides an efficient pathway for the

DOI: 10.1021/acsnano.8b07850
ACS Nano 2019, 13, 1772−1783

Table 1. Summary of Performance of Photodetectors Based on All-Inorganic Perovskite and Nanostructures/Graphene Hybrid Structures

structure	drive voltage (V)	responsivity (A/W)	detectivity (Jones)	rising time/falling time	stability	ref
ITO/$CsPbBr_3$ NS/ITO[a]	10	0.64		0.019 ms/0.024 ms		49
$CsPbBr_3$ NS/CNTs	10	31.1		0.016 ms/0.38 ms		50
$CsPbBr_3$ NPs/Au NCs	2	0.01	4.56×10^8	0.2 ms/1.2 ms		51
ITO/$CsPbBr_3$ MCs/ITO	3	6×10^4	10^{13}	0.5 ms/1.6 ms		52
Au/$CsPbBr_3$ SCs/Au	30	2.1		0.3 s/5 s		53
$CsPbBr_3$ NCs/G	0.2	2×10^4	8.6×10^{10}		320 h	54
Au/$CsPbCl_3$ NCs/Au	10	0.18		1.8 ms/1.0 ms	>1440 h	55
$CsPbCl_3$ NCs/G	0.5	$>10^6$	$>10^{13}$	0.3 s/0.35 s	2400 h	this work

[a]NS, nanosheets; NPs, nanoparticles; MCs, microcrystals; SCs, single crystals; NCs, nanocrystals; G, graphene.

electron injection between them, as evidenced by the much-improved photoresponsivity to be discussed in the following section.

The photoresponsivity (R^*) is an important figure of merit for a photodetector and can be expressed as the photocurrent generated per unit power of absorbed incident light on the active area of $CsPbCl_3$ NCs/GFET photodetector: $R^* = I_{ph}/P_{in}$. The I_{ph} represents the photocurrent equal to the illuminated current under illumination of incident power density (P_{in}) minus dark current. The wavelength-dependent responsivity matches well with the absorption spectrum of the $CsPbCl_3$ NCs coated on a fused silica substrate in Figure 6a with an obvious band edge at about 407 nm. In particular, a sharp edge of the R^* can be observed across the band edge. For example, the responsivity is as high as 7.48×10^5 A/W at 390 nm and decreases by 2 orders of magnitude or more at 430 nm or longer wavelengths. This proves the high crystal quality of the $CsPbCl_3$ NCs with negligible band gap defect states. The extraordinary spectral selectivity of the $CsPbCl_3$ NCs photosensitizers makes the $CsPbCl_3$ NCs/GFET device a good candidate for high-performance, visible-blind UV photodetectors.

The strong quantum confinement of the $CsPbCl_3$ NCs due to small size effects and high carrier mobility of graphene were believed to optimize the photoconductive gain. To quantitatively verify the underlying physical mechanism of the high photoresponsivity, it is necessary to determine the photoconductive gain in the device. The gain in this $CsPbCl_3$ NCs/GFET vdW heterojunction photodetectors can be calculated by the following equation:[46]

$$G = \frac{I_{ph}h\nu}{qiWL} = (a_0 qNVW)\frac{h\nu}{qiWL} = a_0 \varnothing \frac{T_{life}}{T_{transit}} \frac{1}{1 + \left(\frac{i}{i_0}\right)^n} \quad (1)$$

Here, q is the elementary electron charge; i is the light power absorbed by the $CsPbCl_3$ NCs on the GFET channel; L and W are, respectively, the GFET channel length and width; a_0 indicates the photogenerated charge-transfer efficiency from NCs to GFET channel; N is Avogadro's constant; $V = \mu V_{DS}/L$ represents the charge drift velocity; and μ is the charge mobility in graphene. V_{DS} is the source-drain bias voltage, $h\nu$ represents the elemental photon energy (h is the Planck's constant and ν is the photon frequency), $\varnothing$ represents the internal quantum efficiency of $CsPbCl_3$ NCs, T_{life} represents the lifetime of photogenerated carriers, $T_{transit}$ represents the charge transit time in the GFET channel, i_0 represents the saturation light intensity absorbed by the NCs when all of the surface states are filled, and n represents a phenomenological fitting parameter. Figure 6b illustrates the theoretical fitting (red curve) and photoconductive gain of experimental results (black dots) as a function of the light power (i), which was tested on $CsPbCl_3$ NCs/GFET vdW heterojunction devices. It shows an experimental maximum gain of 3.6×10^6 for an optical illumination power of 2.18 pW and demonstrates a monotonic decrease trend with increasing incident light power, which can be ascribed to the saturation of the surface states and the shortening average lifetime of carriers. The theoretical fitting curve (red) agrees well with the experimentally measured gain with the parameters of $a_0\varnothing = 0.20$, $i_0 = 0.70$ pW, and $n = 0.90$. The gain predicted from the theoretical calculation can be reached to $\sim 1.13 \times 10^7$ under a lower incident optical power <0.1 pW. The high photoresponsivity and photoconductive gain demonstrate the promising application perspective of the $CsPbCl_3$ NCs/GFET vdW heterojunction photodetector for practical applications. Figure 6c plots the bias voltage V_{DS}-dependent photoresponsivity, and a high responsivity of $>10^6$ A/W can be obtained on the $CsPbCl_3$ NCs/GFET devices with $V_{DS} \geq 0.5$ V.

Besides the photoresponsivity (R^*) and gain, another important parameter used to characterize a photodetector performance is the specific photodetectivity (D^*), which can be calculated by eq 2:[46]

$$D^* = \frac{\sqrt{S \times \Delta f}}{\mathrm{NEP}} \ (\mathrm{Jones}) \quad (2)$$

where S is the active area of the $CsPbCl_3$ NCs/GFET heterojunction photodetector (cm^2), Δf (Hz) and NEP (A/$Hz^{1/2}$) are the bandwidth and noise equivalent power, respectively. The NEP is a standard metric to demonstrate the sensitivity of the photodetector, which can be obtained by the equation of NEP $= \overline{J_n^2}^{1/2}/R^*$. The mean square noise current $\overline{J_n^2}$ can be obtained from the current noise density spectra of $CsPbCl_3$ NCs/GFET devices (Figure S7). The linearity relationship of the $\overline{J_n^2}$ *vs* frequency can be fitted with $\overline{J_n^2} \propto 1/f$, exhibiting that the $1/f$ noise dominates the current noise signal in the devices in the low-frequency range up to 1 kHz (Figure S7). The source-drain bias voltage-dependent D^* of the $CsPbCl_3$ NCs/GFET photodetectors is shown in Figure 6d. It is found that the D^* could reach to $>2 \times 10^{13}$ Jones at V_{DS} of 1.0 V. The performance and stability results of our $CsPbCl_3$ NCs/GFET photodetectors represents the best performing perovskite/graphene hybrid photodetectors (see Table 1).

DOI: 10.1021/acsnano.8b07850
ACS Nano 2019, 13, 1772−1783

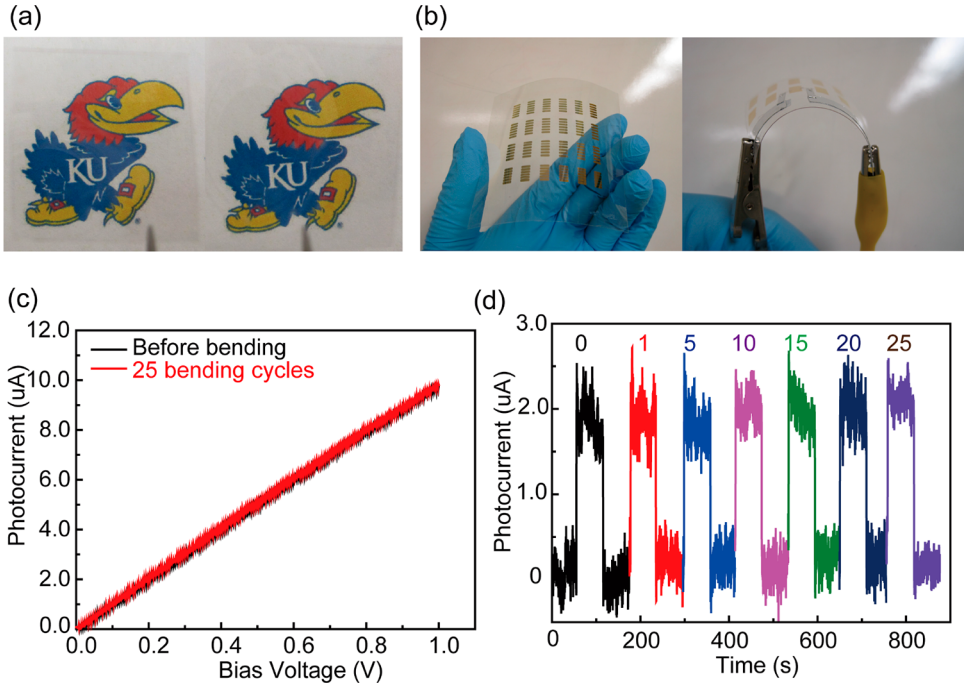

Figure 7. (a) PET flexible substrates before (left) and after (right) coating of $CsPbCl_3$ NCs. Logo reprinted with permission from the University of Kansas (copyright 1947). (b) Digital photograph of the flexible $CsPbCl_3$ NCs/graphene devices. (c) Photocurrent *vs* bias voltage curves of the flexible $CsPbCl_3$ NCs/graphene photodetector before and after 25 bending cycles. (d) Dynamic photoresponse after different numbers of bending cycles.

The ink-based printable process and the adaptability of graphene can enable flexible $CsPbCl_3$ NCs/GFET photodetectors. To certify the viability for flexible device applications, the $CsPbCl_3$ NCs/GFET photodetectors were also fabricated and tested on flexible PET substrates. Figure 7a displays the PET substrates before (left) and after (right) the printing of $CsPbCl_3$ NCs. The high transparency is expected considering the thin layer of the $CsPbCl_3$ NC coating. Figure 7b demonstrates the digital image of the printed devices with the rectangular Au electrodes clearly visible. Up to 25 bending cycles were applied for the investigation of the device stability. Figure 7c shows that the photocurrents stayed unchanged after 25 bending cycles, illustrating the performance of the flexible devices were not affected by bending. The dynamic photocurrent of the photodetector measured after different numbers of bending cycles is shown in Figure 7d, exhibiting superior stability of the flexible devices. These results demonstrate that the $CsPbCl_3$ NCs/graphene heterojunction photodetectors offer excellent stability and are promising for applications in flexible optoelectronic devices.

CONCLUSIONS

In summary, a MPA ligand passivation process has been developed to resolve the critical issues of ambient stability of $CsPbCl_3$ NCs. It has been found that the HS^- ligand, through deprotonation that results in S^{2-} in MPA, can bind firmly to the positively Pb-terminating surface of the $CsPbCl_3$ NCs, which can effectively minimize the ligands loss on the surface of the NCs, resulting in outstanding stability of the $CsPbCl_3$ NCs in ambient. In addition, the MPA passivation of the $CsPbCl_3$ NC surface effectively suppresses charge trapping by the surface defects. This, in combination with the outstanding charge transfer along the MPA ligands, enables high-efficiency charge transfer from $CsPbCl_3$ NCs to other functional materials demonstrated using both DFT simulations and experimental investigation on visible-blind UV $CsPbCl_3$ NCs/GFET photodetectors. On these devices, extraordinary optoelectronic performance has been obtained including high responsivity exceeding 10^6 A/W, detectivity of 2×10^{13} Jones, fast photoresponse within 0.3 s, and ambient stability for more than 2400 h, which represents the best so far achieved on perovskite/graphene hybrid photodetectors. Finally, the entire colloidal process developed in this work for fabrication of the $CsPbCl_3$ NCs/GFET photodetectors can be extended to flexible PET substrates retaining the optoelectronic performance with respect to 25 bending cycles. Therefore, this work provides a practical strategy with which to strengthen the stability and charger-transfer efficiency of inorganic perovskite NCs with great potential applications for scalable and foldable optoelectronic devices.

METHODS

Chemical and Materials. Lead(II) chloride ($PbCl_2$, 99.999% trace metals basis), cesium carbonate (Cs_2CO_3, 99%), 1-octadecene (90%), oleic acid (90%), oleylamine (70%), trioctylphosphine (TOP, 90%), acetone, and hexane (anhydrous, 95%) were bought from Sigma-Aldrich and used without further dilution or modification.

Synthesis of $CsPbCl_3$ NCs. $CsPbCl_3$ NCs were fabricated according to a modified process from a previous reported approach.[8] Briefly, 0.814 g of Cs_2CO_3 was first added to a 100 mL 3-neck round-bottom flask containing 2.5 mL of OA and 40 mL of ODE, and vacuum-pumped and refilled Ar back and forth at 25 °C for 20 min and then increased to 120 °C under an Ar flow with a stirring speed of 600 rpm for 1 h to exclude the moisture in the reaction reagent. In another 3-neck round-bottom flask, we put 0.104 g of $PbCl_2$ into a mixture solution with 1 mL of OLA,1 mL of OA, 2 mL of TOP, and 10 mL of ODE, and we vacuum-pumped and refilled Ar back and forth at temperatures of 25 °C for 20 min and then increased the temperature to 120 °C under an Ar flow with a spinning speed of 600 rpm for 1 h to exclude the moisture in the reaction reagent.

DOI: 10.1021/acsnano.8b07850
ACS Nano 2019, 13, 1772−1783

Thereafter, the above two mixtures were heated to 150 °C under an Ar atmosphere with a constant stirring. A total of 0.8 mL of Cs-oleate precursor solution was then injected rapidly into the second Pb-based precursor. After 10 s of reaction, the reaction was stopped and the reagents cooled to 0 °C rapidly via using an ice−water mixture bath to obtain monodispersed $CsPbCl_3$ NCs with an average size around 10.5 nm. The NCs were obtained by centrifugation at 11 000 rpm for 10 min and cleaned using acetone/hexane mixture solution. The final NCs were stored in a N_2 environment in a glovebox. The UV−vis spectra were also collected on the $CsPbCl_3$ NCs immediately after they were synthesized and 3 months after the storage (Figure S8), which suggest the NCs in storage have negligible degradation.

$CsPbCl_3$ NCs/GFET Photodetector Fabrication. Commercial Si/SiO_2 (90 nm) wafers were used as the substrates. Monolayer graphene was grown using chemical vapor deposition and transferred onto the above Si/SiO_2 substrates as our earlier work.[46] A total of 36 GFETs with different graphene channel sizes of 2−20 μm were patterned using the photolithography method.[47,48] Patterned Au (80 nm)/Ti (2 nm) bars as drain and source contact electrodes were fabricated via an electron-beam evaporator under a high vacuum of 1.0×10^{-7} Torr, followed by lift-off. The $CsPbCl_3$ NCs (5 mg/mL) dissolved in hexane via sonication were used as the printing ink and printed on the patterned GFET channel by using an inkjet microplotter (SonoPlot, Inc.).[46]

$CsPbCl_3$ NCs Surface Engineering. The surface of as-synthesized $CsPbCl_3$ NCs were encapsulated a layer of insulating long carbon chain length molecular OA and OLA, which was effectively replaced by short and highly conductive molecules of MPA. The processing solution was prepared by dissolving and mixing MPA in methanol (50% v/v) in a glove box. The fabricated $CsPbCl_3$ NCs/GFET devices were dipped into the processing solution for different times in the range of 30−120 s at room temperature. The residual processing solution on the surface of $CsPbCl_3$ NCs/GFET devices was washed away by methanol. The final devices were stored in glovebox and dried about 10 min before characterization.

Optical and Optoelectronic Characterization. A UV-3600 Shimadzu was applied to characterize the absorption property of $CsPbCl_3$ NCs. A field-emission FEI Tecnai F20XT was used to take the morphology and nanostructure of the $CsPbCl_3$ NCs. The optical photos of $CsPbCl_3$ NCs/GFET devices were taken from an optical microscope (Nikon Eclipse LV 150). The optoelectronic properties were characterized and recorded via a device analyzer (Agilent B1505A). A xenon lamp with a monochromator system (Newport) provided a tunable light source for the device characterization. The instant power density absorbed by the active layer of $CsPbCl_3$ NCs/GFET devices was calibrated and recorded by a certified Newport power meter. The noise signal of the photodetectors was tested via a spectrum analyzer (Stanford Research SR 760).

ASSOCIATED CONTENT

Supporting Information

The Supporting Information is available free of charge on the ACS Publications website at DOI: 10.1021/acsnano.8b07850.

Additional details regarding the simulation process, SEM results, the photoresponse of $CsPbCl_3$ NCs/GFET photodetectors treated with methanol only, and current noise density spectra (PDF)

AUTHOR INFORMATION

Corresponding Authors

*E-mail: gmg@ku.edu.
*E-mail: jwu@ku.edu.

ORCID

Maogang Gong: 0000-0002-2031-781X
Judy Z. Wu: 0000-0001-7040-4420

Notes

The authors declare no competing financial interest.

ACKNOWLEDGMENTS

The authors are thankful for the support by Plant Directed Research and Development funds from the Department of Energy's National Security Campus, operated and managed by Honeywell Federal Manufacturing and Technologies, LLC under contract no. DE-NA0002839. This research also funded by NSF contract nos. NSF-DMR-1508494 and NSF-ECCS-1809293/1809284 and ARO contract no. W911NF-16-1-0029.

REFERENCES

(1) Lee, Y.; Kwon, J.; Hwang, E.; Ra, C.-H.; Yoo, W. J.; Ahn, J.-H.; Park, J. H.; Cho, J. H. High-Performance Perovskite−Graphene Hybrid Photodetector. *Adv. Mater.* **2015**, *27*, 41−46.

(2) Wang, Y.; Zhang, Y.; Lu, Y.; Xu, W.; Mu, H.; Chen, C.; Qiao, H.; Song, J.; Li, S.; Sun, B.; Cheng, Y.-B.; Bao, Q. Hybrid Graphene−Perovskite Phototransistors with Ultrahigh Responsivity and Gain. *Adv. Opt. Mater.* **2015**, *3*, 1389−1396.

(3) Nie, W. Y.; Tsai, H. H.; Asadpour, R.; Blancon, J. C.; Neukirch, A. J.; Gupta, G.; Crochet, J. J.; Chhowalla, M.; Tretiak, S.; Alam, M. A.; Wang, H. L.; Mohite, A. D. High-Efficiency Solution-Processed Perovskite Solar Cells with Millimeter-Scale Grains. *Science* **2015**, *347*, 522−525.

(4) Green, M. A.; Ho-Baillie, A.; Snaith, H. J. The Emergence of Perovskite Solar Cells. *Nat. Photonics* **2014**, *8*, 506−514.

(5) Xing, G.; Mathews, N.; Sun, S.; Lim, S. S.; Lam, Y. M.; Gratzel, M.; Mhaisalkar, S.; Sum, T. C. Long-Range Balanced Electron- and Hole-Transport Lengths in Organic-Inorganic $CH_3NH_3PbI_3$. *Science* **2013**, *342*, 344−347.

(6) Kovalenko, M. V.; Protesescu, L.; Bodnarchuk, M. I. Properties and Potential Optoelectronic Applications of Lead Halide Perovskite Nanocrystals. *Science* **2017**, *358*, 745−750.

(7) Akkerman, Q. A.; Raino, G.; Kovalenko, M. V.; Manna, L. Genesis, Challenges and Opportunities for Colloidal Lead Halide Perovskite Nanocrystals. *Nat. Mater.* **2018**, *17*, 394−405.

(8) Protesescu, L.; Yakunin, S.; Bodnarchuk, M. I.; Krieg, F.; Caputo, R.; Hendon, C. H.; Yang, R. X.; Walsh, A.; Kovalenko, M. V. Nanocrystals of Cesium Lead Halide Perovskites ($CsPbX_3$, X = Cl, Br, and I): Novel Optoelectronic Materials Showing Bright Emission with Wide Color Gamut. *Nano Lett.* **2015**, *15*, 3692−3696.

(9) Li, X.; Cao, F.; Yu, D.; Chen, J.; Sun, Z.; Shen, Y.; Zhu, Y.; Wang, L.; Wei, Y.; Wu, Y.; Zeng, H. All Inorganic Halide Perovskites Nanosystem: Synthesis, Structural Features, Optical Properties and Optoelectronic Applications. *Small* **2017**, *13*, 1603996.

(10) Li, X.; Liu, Y.; Song, X.; Wang, H.; Gu, H.; Zeng, H. Intercrossed Carbon Nanorings with Pure Surface States as Low-Cost and Environment-Friendly Phosphors for White-Light-Emitting Diodes. *Angew. Chem., Int. Ed.* **2015**, *54*, 1759−1764.

(11) Song, J.; Li, J.; Li, X.; Xu, L.; Dong, Y.; Zeng, H. Quantum Dot Light-Emitting Diodes Based on Inorganic Perovskite Cesium Lead Halides ($CsPbX_3$). *Adv. Mater.* **2015**, *27*, 7162−7167.

(12) Li, J.; Xu, L.; Wang, T.; Song, J.; Chen, J.; Xue, J.; Dong, Y.; Cai, B.; Shan, Q.; Han, B.; Zeng, H. 50-Fold EQE Improvement up to 6.27% of Solution-Processed All-Inorganic Perovskite $CsPbBr_3$ QLEDs *via* Surface Ligand Density Control. *Adv. Mater.* **2017**, *29*, 1603885.

(13) Lin, K.; Xing, J.; Quan, L. N.; de Arquer, F. P. G.; Gong, X.; Lu, J.; Xie, L.; Zhao, W.; Zhang, D.; Yan, C.; Li, W.; Liu, X.; Lu, Y.; Kirman, J.; Sargent, E. H.; Xiong, Q.; Wei, Z. Perovskite Light-Emitting Diodes with External Quantum Efficiency Exceeding 20%. *Nature* **2018**, *562*, 245−248.

(14) Wang, Y.; Li, X.; Song, J.; Xiao, L.; Zeng, H.; Sun, H. All-Inorganic Colloidal Perovskite Quantum Dots: A New Class of Lasing Materials with Favorable Characteristics. *Adv. Mater.* **2015**, *27*, 7101−7108.

DOI: 10.1021/acsnano.8b07850
ACS Nano 2019, 13, 1772−1783

(15) Zhang, Q.; Su, R.; Du, W.; Liu, X.; Zhao, L.; Ha, S. T.; Xiong, Q. Advances in Small Perovskite-Based Lasers. *Small Methods* **2017**, *1*, 1700163.
(16) Su, R.; Diederichs, C.; Wang, J.; Liew, T. C. H.; Zhao, J.; Liu, S.; Xu, W.; Chen, Z.; Xiong, Q. Room-Temperature Polariton Lasing in All-Inorganic Perovskite Nanoplatelets. *Nano Lett.* **2017**, *17*, 3982−3988.
(17) Sutton, R. J.; Eperon, G. E.; Miranda, L.; Parrott, E. S.; Kamino, B. A.; Patel, J. B.; Hörantner, M. T.; Johnston, M. B.; Haghighirad, A. A.; Moore, D. T.; Snaith, H. J. Bandgap-Tunable Cesium Lead Halide Perovskites with High Thermal Stability for Efficient Solar Cells. *Adv. Energy Mater.* **2016**, *6*, 1502458.
(18) Sanehira, E. M.; Marshall, A. R.; Christians, J. A.; Harvey, S. P.; Ciesielski, P. N.; Wheeler, L. M.; Schulz, P.; Lin, L. Y.; Beard, M. C.; Luther, J. M. Enhanced Mobility $CsPbI_3$ Quantum Dot Arrays for Record-Efficiency, High-Voltage Photovoltaic Cells. *Sci. Adv.* **2017**, *3*, 4204.
(19) Ramasamy, P.; Lim, D. H.; Kim, B.; Lee, S. H.; Lee, M. S.; Lee, J. S. All-Inorganic Cesium Lead Halide Perovskite Nanocrystals for Photodetector Applications. *Chem. Commun.* **2016**, *52*, 2067−2070.
(20) Wang, S.; Wang, K.; Gu, Z.; Wang, Y.; Huang, C.; Yi, N.; Xiao, S.; Song, Q. Solution-Phase Synthesis of Cesium Lead Halide Perovskite Microrods for High-Quality Microlasers and Photodetectors. *Adv. Opt. Mater.* **2017**, *5*, 1700023.
(21) Huang, H.; Polavarapu, L.; Sichert, J. A.; Susha, A. S.; Urban, A. S.; Rogach, A. L. Colloidal Lead Halide Perovskite Nanocrystals: Synthesis, Optical Properties and Applications. *NPG Asia Mater.* **2016**, *8*, e328−e328.
(22) Krieg, F.; Ochsenbein, S. T.; Yakunin, S.; Ten Brinck, S.; Aellen, P.; Suess, A.; Clerc, B.; Guggisberg, D.; Nazarenko, O.; Shynkarenko, Y.; Kumar, S.; Shih, C. J.; Infante, I.; Kovalenko, M. V. Colloidal $CsPbX_3$ (X = Cl, Br, I) Nanocrystals 2.0: Zwitterionic Capping Ligands for Improved Durability and Stability. *ACS Energy Lett.* **2018**, *3*, 641−646.
(23) Koscher, B. A.; Swabeck, J. K.; Bronstein, N. D.; Alivisatos, A. P. Essentially Trap-Free $CsPbBr_3$ Colloidal Nanocrystals by Postsynthetic Thiocyanate Surface Treatment. *J. Am. Chem. Soc.* **2017**, *139*, 6566−6569.
(24) Pan, J.; Quan, L. N.; Zhao, Y.; Peng, W.; Murali, B.; Sarmah, S. P.; Yuan, M.; Sinatra, L.; Alyami, N. M.; Liu, J.; Yassitepe, E.; Yang, Z.; Voznyy, O.; Comin, R.; Hedhili, M. N.; Mohammed, O. F.; Lu, Z. H.; Kim, D. H.; Sargent, E. H.; Bakr, O. M. Highly Efficient Perovskite-Quantum-Dot Light-Emitting Diodes by Surface Engineering. *Adv. Mater.* **2016**, *28*, 8718−8725.
(25) Pan, J.; Shang, Y.; Yin, J.; De Bastiani, M.; Peng, W.; Dursun, I.; Sinatra, L.; El-Zohry, A. M.; Hedhili, M. N.; Emwas, A. H.; Mohammed, O. F.; Ning, Z.; Bakr, O. M. Bidentate Ligand-Passivated $CsPbI_3$ Perovskite Nanocrystals for Stable near-Unity Photoluminescence Quantum Yield and Efficient Red Light-Emitting Diodes. *J. Am. Chem. Soc.* **2018**, *140*, 562−565.
(26) Zhou, Q.; Bai, Z.; Lu, W. G.; Wang, Y.; Zou, B.; Zhong, H. *In Situ* Fabrication of Halide Perovskite Nanocrystal-Embedded Polymer Composite Films with Enhanced Photoluminescence for Display Backlights. *Adv. Mater.* **2016**, *28*, 9163−9168.
(27) Huang, H.; Chen, B.; Wang, Z.; Hung, T. F.; Susha, A. S.; Zhong, H.; Rogach, A. L. Water Resistant $CsPbX_3$ Nanocrystals Coated with Polyhedral Oligomeric Silsesquioxane and Their Use as Solid State Luminophores in All-Perovskite White Light-Emitting Devices. *Chem. Sci.* **2016**, *7*, 5699−5703.
(28) Li, Z.; Kong, L.; Huang, S.; Li, L. Highly Luminescent and Ultrastable $CsPbBr_3$ Perovskite Quantum Dots Incorporated into a Silica/Alumina Monolith. *Angew. Chem., Int. Ed.* **2017**, *56*, 8134−8138.
(29) Pan, A.; He, B.; Fan, X.; Liu, Z.; Urban, J. J.; Alivisatos, A. P.; He, L.; Liu, Y. Insight into the Ligand-Mediated Synthesis of Colloidal $CsPbBr_3$ Perovskite Nanocrystals: The Role of Organic Acid, Base, and Cesium Precursors. *ACS Nano* **2016**, *10*, 7943−7954.
(30) De Roo, J.; Ibanez, M.; Geiregat, P.; Nedelcu, G.; Walravens, W.; Maes, J.; Martins, J. C.; Van Driessche, I.; Kovalenko, M. V.; Hens, Z. Highly Dynamic Ligand Binding and Light Absorption Coefficient of Cesium Lead Bromide Perovskite Nanocrystals. *ACS Nano* **2016**, *10*, 2071−2081.
(31) Ahmed, G. H.; Yin, J.; Bose, R.; Sinatra, L.; Alarousu, E.; Yengel, E.; AlYami, N. M.; Saidaminov, M. I.; Zhang, Y.; Hedhili, M. N.; Bakr, O. M.; Brédas, J.-L.; Mohammed, O. F. Pyridine-Induced Dimensionality Change in Hybrid Perovskite Nanocrystals. *Chem. Mater.* **2017**, *29*, 4393−4400.
(32) Tan, Y.; Zou, Y.; Wu, L.; Huang, Q.; Yang, D.; Chen, M.; Ban, M.; Wu, C.; Wu, T.; Bai, S.; Song, T.; Zhang, Q.; Sun, B. Highly Luminescent and Stable Perovskite Nanocrystals with Octylphosphonic Acid as a Ligand for Efficient Light-Emitting Diodes. *ACS Appl. Mater. Interfaces* **2018**, *10*, 3784−3792.
(33) Song, J.; Li, J.; Xu, L.; Li, J.; Zhang, F.; Han, B.; Shan, Q.; Zeng, H. Room-Temperature Triple-Ligand Surface Engineering Synergistically Boosts Ink Stability, Recombination Dynamics, and Charge Injection toward Eqe-11.6% Perovskite QLEDs. *Adv. Mater.* **2018**, *30*, No. 1800764.
(34) Song, J.; Fang, T.; Li, J.; Xu, L.; Zhang, F.; Han, B.; Shan, Q.; Zeng, H. Organic-Inorganic Hybrid Passivation Enables Perovskite QLEDs with an EQE of 16.48%. *Adv. Mater.* **2018**, *30*, 1805409.
(35) Wang, C.; Chesman, A. S.; Jasieniak, J. J. Stabilizing the Cubic Perovskite Phase of $CsPbI_3$ Nanocrystals by Using an Alkyl Phosphinic Acid. *Chem. Commun.* **2017**, *53*, 232−235.
(36) Yang, D.; Li, X.; Zeng, H. Surface Chemistry of All Inorganic Halide Perovskite Nanocrystals: Passivation Mechanism and Stability. *Adv. Mater. Interfaces* **2018**, *5*, 1701662.
(37) Gong, M.; Sakidja, R.; Liu, Q.; Goul, R.; Ewing, D.; Casper, M.; Stramel, A.; Elliot, A.; Wu, J. Z. Broadband Photodetectors Enabled by Localized Surface Plasmonic Resonance in Doped Iron Pyrite Nanocrystals. *Adv. Opt. Mater.* **2018**, *6*, 1701241.
(38) Ip, A. H.; Thon, S. M.; Hoogland, S.; Voznyy, O.; Zhitomirsky, D.; Debnath, R.; Levina, L.; Rollny, L. R.; Carey, G. H.; Fischer, A.; Kemp, K. W.; Kramer, I. J.; Ning, Z.; Labelle, A. J.; Chou, K. W.; Amassian, A.; Sargent, E. H. Hybrid Passivated Colloidal Quantum Dot Solids. *Nat. Nanotechnol.* **2012**, *7*, 577−582.
(39) Zhitomirsky, D.; Voznyy, O.; Levina, L.; Hoogland, S.; Kemp, K. W.; Ip, A. H.; Thon, S. M.; Sargent, E. H. Engineering Colloidal Quantum Dot Solids within and Beyond the Mobility-Invariant Regime. *Nat. Commun.* **2014**, *5*, 3803.
(40) Qin, L.; Wu, L.; Kattel, B.; Li, C.; Zhang, Y.; Hou, Y.; Wu, J.; Chan, W.-L. Using Bulk Heterojunctions and Selective Electron Trapping to Enhance the Responsivity of Perovskite-Graphene Photodetectors. *Adv. Funct. Mater.* **2017**, *27*, 1704173.
(41) Wu, L.; Qin, L.; Zhang, Y.; Alamri, M.; Gong, M.; Zhang, W.; Zhang, D.; Chan, W. L.; Wu, J. Z. High-Sensitivity Light Detection *via* Gate Tuning of Organometallic Perovskite/PCBM Bulk Heterojunctions on Ferroelectric $Pb_{0.92}La_{0.08}Zr_{0.52}Ti_{0.48}O_3$ Gated Graphene Field Effect Transistors. *ACS Appl. Mater. Interfaces* **2018**, *10*, 12824−12830.
(42) Lin, Q.; Yun, H. J.; Liu, W.; Song, H. J.; Makarov, N. S.; Isaienko, O.; Nakotte, T.; Chen, G.; Luo, H.; Klimov, V. I.; Pietryga, J. M. Phase-Transfer Ligand Exchange of Lead Chalcogenide Quantum Dots for Direct Deposition of Thick, Highly Conductive Films. *J. Am. Chem. Soc.* **2017**, *139*, 6644−6653.
(43) Zhang, X.; Zhou, Q.; Huang, Y.; Li, Z.; Zhang, Z. Contrastive Analysis of the Raman Spectra of Polychlorinated Benzene: Hexachlorobenzene and Benzene. *Sensors* **2011**, *11*, 11510−11515.
(44) El Mendili, Y.; Grasset, F.; Randrianantoandro, N.; Nerambourg, N.; Greneche, J.-M.; Bardeau, J.-F. Improvement of Thermal Stability of Maghemite Nanoparticles Coated with Oleic Acid and Oleylamine Molecules: Investigations under Laser Irradiation. *J. Phys. Chem. C* **2015**, *119*, 10662−10668.
(45) Czamara, K.; Majzner, K.; Pacia, M. Z.; Kochan, K.; Kaczor, A.; Baranska, M. Raman Spectroscopy of Lipids: A Review. *J. Raman Spectrosc.* **2015**, *46*, 4−20.
(46) Gong, M.; Liu, Q.; Cook, B.; Kattel, B.; Wang, T.; Chan, W. L.; Ewing, D.; Casper, M.; Stramel, A.; Wu, J. Z. All-Printable ZnO Quantum Dots/Graphene Van Der Waals Heterostructures for

DOI: 10.1021/acsnano.8b07850
ACS Nano 2019, 13, 1772−1783

Ultrasensitive Detection of Ultraviolet Light. *ACS Nano* **2017**, *11*, 4114−4123.
(47) Xu, G.; Lu, R.; Liu, J.; Chiu, H.-Y.; Hui, R.; Wu, J. Photodetection Based on Ionic Liquid Gated Plasmonic Ag Nanoparticle/Graphene Nanohybrid Field Effect Transistors. *Adv. Opt. Mater.* **2014**, *2*, 729−736.
(48) Lu, R. T.; Liu, J. W.; Luo, H. F.; Chikan, V.; Wu, J. Z. Graphene/Gase-Nanosheet Hybrid: Towards High Gain and Fast Photoresponse. *Sci. Rep.* **2016**, *6*, 19161.
(49) Song, J.; Xu, L.; Li, J.; Xue, J.; Dong, Y.; Li, X.; Zeng, H. Monolayer and Few-Layer All-Inorganic Perovskites as a New Family of Two-Dimensional Semiconductors for Printable Optoelectronic Devices. *Adv. Mater.* **2016**, *28*, 4861−4869.
(50) Li, X.; Yu, D.; Chen, J.; Wang, Y.; Cao, F.; Wei, Y.; Wu, Y.; Wang, L.; Zhu, Y.; Sun, Z.; Ji, J.; Shen, Y.; Sun, H.; Zeng, H. Constructing Fast Carrier Tracks into Flexible Perovskite Photodetectors to Greatly Improve Responsivity. *ACS Nano* **2017**, *11*, 2015−2023.
(51) Dong, Y.; Gu, Y.; Zou, Y.; Song, J.; Xu, L.; Li, J.; Xue, J.; Li, X.; Zeng, H. Improving All-Inorganic Perovskite Photodetectors by Preferred Orientation and Plasmonic Effect. *Small* **2016**, *12*, 5622−5632.
(52) Yang, B.; Zhang, F.; Chen, J.; Yang, S.; Xia, X.; Pullerits, T.; Deng, W.; Han, K. Ultrasensitive and Fast All-Inorganic Perovskite-Based Photodetector *via* Fast Carrier Diffusion. *Adv. Mater.* **2017**, *29*, 1703758.
(53) Cha, J. H.; Han, J. H.; Yin, W.; Park, C.; Park, Y.; Ahn, T. K.; Cho, J. H.; Jung, D. Y. Photoresponse of $CsPbBr_3$ and Cs_4PbBr_6 Perovskite Single Crystals. *J. Phys. Chem. Lett.* **2017**, *8*, 565−570.
(54) Chen, J.-h.; Jing, Q.; Xu, F.; Lu, Z.-d.; Lu, Y.-q. High-Sensitivity Optical-Fiber-Compatible Photodetector with an Integrated $CsPbBr_3$−Graphene Hybrid Structure. *Optica* **2017**, *4*, 835−838.
(55) Li, X.; Yu, D.; Cao, F.; Gu, Y.; Wei, Y.; Wu, Y.; Song, J.; Zeng, H. Healing All-Inorganic Perovskite Films *via* Recyclable Dissolution-Recyrstallization for Compact and Smooth Carrier Channels of Optoelectronic Devices with High Stability. *Adv. Funct. Mater.* **2016**, *26*, 5903−5912.

DOI: 10.1021/acsnano.8b07850
ACS Nano 2019, 13, 1772−1783